Title

Comparison of sparse domain approaches for 4D SPECT dynamic image reconstruction

Journal

Medical Physics, 45(10)

ISSN

0094-2405

Authors

Mitra, Debasis

Abdalah, Mahmoud

Boutchko, Rostyslav

et al.

Publication Date

2018-10-01

DOI

10.1002/mp.13099

Peer reviewed

Comparison of Sparse Domain Approaches for 4D SPECT Dynamic Image Reconstruction

Debasis Mitra[1], Mahmoud Abdalah[2], Rostyslav Boutchko[3], Haoran Chan[1], Uttam Shrestha[4], Elias Botvinick[4], Youngho Seo[4], Grant T. Gullberg[4]

[1]Florida Institute of Technology, [2]Moffitt Cancer Center, [3]Lawrence Berkeley National Lab, [4]University of California San Francisco

E-mail[1]: dmitra@cs.fit.edu

Abstract. ***Purpose***: Dynamic imaging (DI) provides additional diagnostic information in emission tomography in comparison to conventional static imaging at the cost of being computationally more challenging. Dynamic SPECT (Single Photon Emission Computed Tomography) reconstruction is particularly hard because of the limitations in sampling geometry present in most existing scanners. We have presented an algorithm *Spline Initialized Factor Analysis of Dynamic Structures* (SIFADS) that is a matrix factorization method for reconstructing the dynamics of tracers in tissues and blood directly from the projections in dynamic cardiac SPECT, without first resorting to any 3D reconstruction. ***Methods****:* SIFADS is different from "pure" FADS in that it employs a dedicated spline-based pre-initialization. In this paper, we analyze the convergence properties of SIFADS and FADS using multiple metrics. The performances of the two approaches are evaluated for numerically simulated data and for real dynamic SPECT data from canine and human subjects. ***Results****:* Most reconstruction algorithm convergence metrics analyzed here show better curve features over iterations, or better tissue segmentations, for SIAFDS than pure FADS. Computational times measured are also typically

better for SIFADS implementations over those with pure FADS. ***Conclusion****:* The analysis supports the utility of the pre-initialization of factorization algorithm for better dynamic SPECT image reconstruction.

Abbreviations: FADS: factor analysis with dynamic structures; SIFADS: spline-initialized FADS; TAC: time activity curve; LV: left ventricle; RV: right ventricle

1. INTRODUCTION

In conventional static nuclear imaging, one assumes equilibrium in tracer concentration and reconstructs a three dimensional image of the accumulated tracer distribution. Dynamic imaging extends beyond that and probes dynamic properties of the tracer by measuring the tracer distribution as it changes with time from the moment of injection. We have shown previously how to obtain direct organ segmentation based on the respective tracer dynamics for both SPECT[1] and PET (Positron Emission Tomography)[2], by applying a known matrix factorization technique[3] called factor analysis in dynamic structures (FADS)[4]. One of the novelties we claimed for SPECT reconstruction directly from the projections was that often we can recover the blood input function and other time activity curves, which was not generally available from post-reconstruction region-of-interest (ROI) sampling in conventional approaches providing three dimensional reconstructed temporal images. In this work we further study our algorithm's convergence properties on more extensive sets of data.

There have been several works published about dynamic cardiac SPECT using various cameras: three headed cameras,[5] two headed large field of view cameras,[6-9] two headed large field of view cameras with diagnostic CT,[10] and new dedicated cameras using CZT.[11-13] With these various cameras, dynamic cardiac SPECT has been performed with various tracers, including: ^{201}Tl,[14] ^{99m}Tc-teboroxime,[5,15-18] ^{99m}Tc-sestamibi,[8] and ^{99m}Tc-tetrofosmin.[9,13] Recently work has shown that dynamic SPECT has promise for measuring flow and CFR with large field of view gamma cameras.[8,10,19-21] However, in all of these works it is recognized that because of slow camera rotation, dynamic data must be reconstructed directly from the

projections themselves, that is, performing 4D reconstruction[1,6,7,9,22] with appropriate corrections for attenuation, partial volume, and scatter.[23-25]

Algorithms have advanced,[26] including modeling of cardiac motion in dynamic 5D reconstruction,[27,28] modeling of cardiac and respiratory motion in dynamic 6D reconstruction [Shrestha],[29] and directly fitting compartment models.[30] Our SIFADS method[1,31] [Alhassen??[20]] is a 4D reconstruction approach that directly estimates time activity curves (TACs) from projections of dynamic data acquired from slowly rotating gamma cameras and differs from these previous methods where first dynamic image frames are reconstructed, and then, from which TACs can be generated. Our method, first uses splines to obtain an initial solution for a FADS algorithm that estimates the desired TACs. The method involves segmenting the tissues based on their dynamics and involves a similar approach as proposed by Zan et al.[32] via reduction in spatial and temporal dimensions. The SIFADS method can be further extended to address cardiac motion.

Dynamic SPECT imaging with slow gantry rotation involves camera heads rotating while the tracer concentration is temporally changing due to tracer kinetics. Direct reconstruction from the projection data is the only way to describe tracer dynamics immediately following the injection, since a dynamic sequence of static 3D reconstructions is not feasible[4,10,20,33,34] because of data inconsistencies. FADS approach[4] is possibly the only way to address this problem. However, such matrix factorization techniques are known to be dependent on solution initialization. SIFADS addresses that by using a spline-based initialization technique. This approach of initialization acts also as generic method for estimation of tracer dynamics without being sensitive to which tracer is actually being used in experiments. This leads to better quantitative and qualitative results in reconstruction of time activity curves as evidenced from our results.

Our method is an alternative to kinetic modeling[6,35], which is a popular approach in dynamic nuclear imaging, and is not exactly comparable. We segment the tissues based on their dynamics and do not study their diffusion between blood and tissue types. A detailed study on cohorts to show which approach is better for diagnosis: ours or the standard kinetic parameter estimation, is beyond the scope of this work. Accuracy measurements presented in this work are similar to those of Jin et al.[28].

SIFADS differs from that work in factor initialization[5] and regularization regime,[36] and our work does not address cardiac or any motion at this stage.[28,37]

The paper is organized as follows. In Section 2, we present the algorithm and some measures that we use in the current work to evaluate the algorithm's performance. We also describe in this section methods used to generate simulated data and to acquire canine and human SPECT projection data. The results of our work and a conclusion are provided in Sections 3 and 4, respectively.

2. METHODS

2.1. Algorithm

The forward problem in our dynamic reconstruction is:

$$P_n = \sum_k S_{nk} V_k(t) \quad P_n = \sum_i S_{ki} V_i(t), \tag{1}$$

where P_n are the projection bins that depend on time (one projection view angle per time instance), S_{nk} are the elements of the (sparse) system matrix, and $V_k(t)$ are the time-dependent voxel intensities to be determined, n runs on detector bins whereas k runs on image voxels. In order to solve this problem, the time-dependent volume is factorized:

$$V_{k,t} = \sum_j C_{kj} f_{j,t} \quad V_j = \sum_j C_{ij} f_{jt}, \tag{2}$$

with t the index of discretized time; $j \in [1, J]$ the index of the factor f from a set of J one-dimensional time series acting as expansion basis functions for factorization (typically $J \sim$ 3-5), and C the spatially discretized distribution of factor expansion coefficients. Each estimated C is thresholded using Otsu's method.[38] Thresholded coefficients represent segmentation of the tissues based on the respective temporal dynamics, and the corresponding factors f represent estimated temporal dynamics). Note that the index t addresses both time points and equivalently, the subset of projection bin indices n corresponding to the gantry rotation angle for the SPECT camera. SPECT system matrices in our work were generated by us from the acquisition parameters and collimator specification with a Gaussian point spread

function. Attenuation coefficients were used for real data, but not in the case of simulation data. No scatter correction was used in this work.

In a pure spline-based method[39], *f* is a fixed set of b-splines. The optimization procedure estimates only the coefficients *C* (Fig. 1A). In pure FADS[4,5,40,41], both *C* and *f arrays* are estimated from *P* and *S*, with the optimization algorithm iteratively searching alternately for *C* and for *f* (Fig. 1B). For this pure FADS initialization of *f* vectors are with b-splines but initialization of *C* matrix may be with arbitrary values, and we initialize with all ones. The primary limitations of these methods are reliance on the correct choice of initial temporal basis functions for the pure spline-based approach, and high sensitivity to factor initialization and high likelihood of converging to a local minimum for FADS. These methods are types of a *non-negative matrix factorization* approach[3] that is known to be very sensitive to initialization. FADS method is also similar to *dictionary learning* in image processing[42,43].

We show the spline-based method in Fig. 1A as we use it as pre-initialization process within SIFADS, and the pure FADS in Fig. 1B, which constitutes the essence of SIFADS. The purpose of developing SIFADS is to find a way to initialize FADS better with spline-based method. Fig 1C shows how these two algorithms are used within SIFADS. The top right side of Fig. 1C is where the spline-based method produces initial values for the subsequent FADS part (the bottom three steps Fig 1c). SIFADS mitigates the problem of both the pure spline-based method and the arbitrarily initialized FADS method by first using a few iterations of the spline-based method (typically, 3-5 iterations) in order to initialize (*C* and corresponding *f* arrays) and, subsequently, performs FADS. The result is a robust and more reliable method as described in[1].

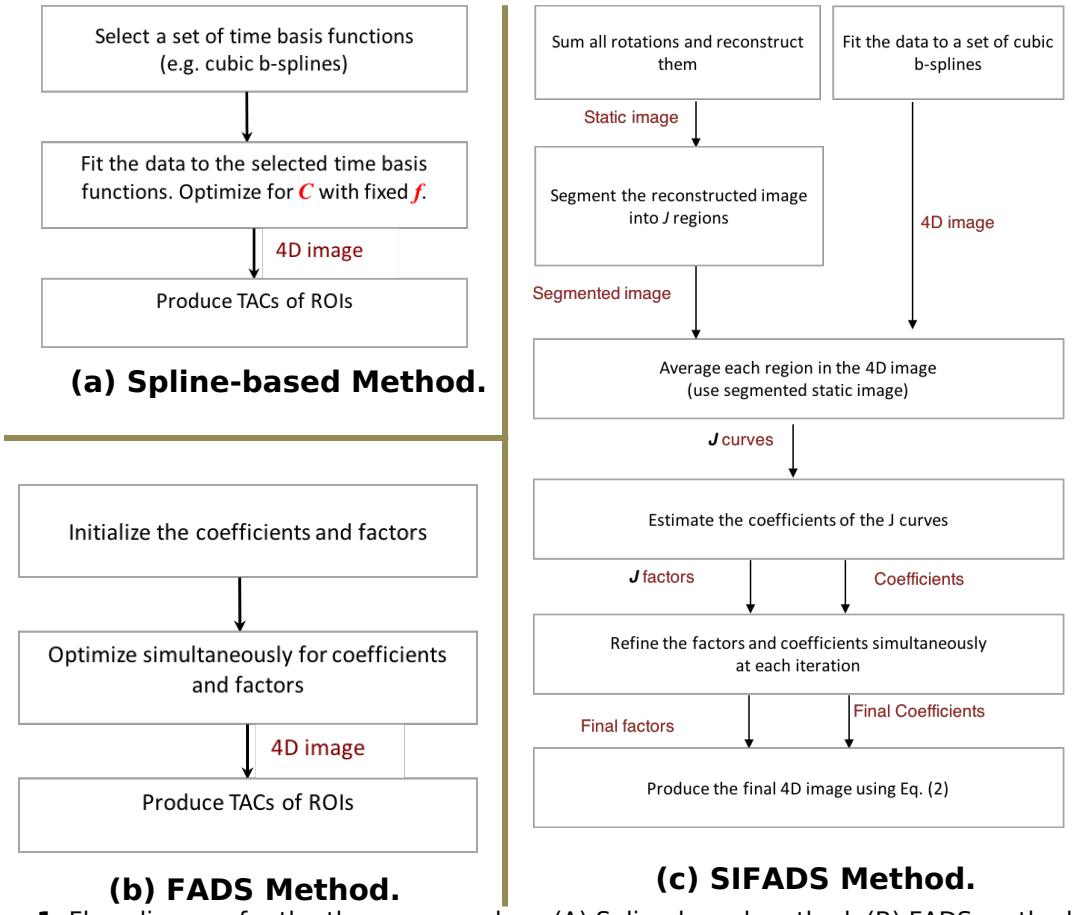

Figure 1: Flow diagram for the three approaches. (A) Spline-based method. (B) FADS method. (C) SIFADS method.

In order to quantify the performance differences between SIFADS and its predecessors, we apply the algorithm to three dynamic cardiac SPECT datasets: simulated data using an XCAT phantom, a canine dynamic imaging study, and a human dynamic imaging study. In order to have a fair comparison, we initialize all algorithms with the same b-splines. In pure FADS the number of TACs may differ from the number of initial b-splines based on how many regions for which we want to estimate TACs. The final estimated TAC for each segment is the average over all the TACs of the voxels in that segment. Each segment is obtained by segmentation of the 3D image reconstructed from later projections (usually projections are almost consistent 4.5 to 30 minutes after tracer injection) of the same SPECT data acquisition. Maximum likelihood expectation maximization (MLEM) algorithm, or rather its regularized version, *maximum a-posterior* (MAP) algorithm[44] with *anisotropic total variation*[45], is used for this static reconstruction. The earlier

tomographic rotations are used for the dynamic reconstruction (inconsistent projections from 0 to 4.5 minutes after tracer injection).

2.2. Performance Measures

The following measures are used to evaluate the performance of the algorithm as a function of the iteration: projection error, a posterior function, convergence estimate, and TAC curve error. All of these measures (except CPU time) are dimensionless.

2.2.1. The *mean square projection distance* computes how close the estimated projections are to the measured projections. In the absence of the ground truth, this quantity serves as the most direct estimate of the validity. This distance should never become zero except for noise-free simulated projections of a smooth distribution, as the projection/ backprojections generally reduces noise and smoothens the signal noise:

$$Error\ Distance = \frac{1}{N}\sum_{n=1}^{N}\left(sinogram_{True} - sinogram_{est}\right)^2 \quad . \tag{3}$$

2.2.2. The *a-posterior function* is the objective function in the MAP reconstruction[45] that estimates the likelihood of the reconstructed image taking into account the acquired projections and the prior information:

$$L(C,f) = \sum_n \left(-\left(\sum_k S_{nk} \sum_j C_{kj} f_{j,t} \right) + P_n \ln\left(\sum_k S_{nk} \sum_j C_{kj} f_{j,t} \right) + \ln\left(P_n!\right) \right) - U(C,f), \tag{4}$$

where $U(C,f) = \Omega(c) + \Theta(c) + \Theta(f)$ is a prior function that describes the available a-priori knowledge about C and f. We use two types of regularizing functions within U, *one for spatial regularization and one for temporal regularization*, described in more detail in Abdalah et al.[1] Spatial regularization is applied to the coefficients C and includes two penalty functions. One function for preventing the coefficients from being mixed together in the same voxel, i.e. we prefer each voxel to be of one tissue type. This is managed by minimizing the dot product between coefficients[42]. For more detail on this penalty function one may refer Abdalah et al.[1,31]

$$\Omega(c)=\sum_{k,j}\sum_{l\vee l\neq j}^{J}(C_{k,j}.C_{k,l}¿)¿. \quad (5)$$

The second penalty is an *anisotropic (tissue-specific) total variation* function to enforce spatial smoothness[45].

$$\Theta(c)=\sum_{k,j}\sum_{n\in\{N_k\}}\left|C_{k,j}-C_{n,j}\right|, \quad (6)$$

where $\{N_k\}$ is the set of the k^{th} voxel's immediate neighbors. The temporal regularization function is applied to the estimated factor curves f to enforce their smoothness. We use the *L_1-norm* for the smoothness penalty functions that is more robust against outliers.[45,46]

$$\Theta(f)=\sum_{j=1}^{J}\sum_{t=2}^{T}\left|f_{j,t}-f_{j,t-1}\right|. \quad (7)$$

Even though our results (in subsequent sections) show that SIFADS does not always converges to lower objective function values compared that of FADS, we still used this measure in the study to have the playing field level. Objective function in both the algorithm is same and this is the only measure that the optimization algorithm is "aware" of. We discuss the implication of our results later in this paper.

2.2.3. In order to measure the iteration-wise *degree of convergence* of the coefficients $C_{k,j}$ (independent of its accuracy), we use the asymptotic mean ratio of the reconstructed voxel values to the values of the same voxels in the previous iteration of the algorithm:

$$Convergence_i=\frac{1}{J\times K}\left(\sum_{j}^{J}\sum_{k=1}^{K}\frac{C_{k,j}^{i}}{C_{k,j}^{i-1}}\right) . \quad (8)$$

At the *i*-th iteration the convergence value is equal to the sum of the current measured coefficient value divided by the coefficient value from the previous iteration, where *k* is the voxel index and *j* is the factor index. However, this measure has to be interpreted with care as only non-zero voxels participate in this computation. The number of non-zero voxels on the boundary of precision (with respect to an arbitrarily assigned low threshold used by us) fluctuates from iteration

to iteration. In essence, this measure produces a combined effect of zero elimination and voxel-convergence.

2.2.4. When the ground truth is available, as in the simulated dynamic projection data generated from XCAT phantom,[47] we also measure the accuracy of the TACs by calculating the relative *root-mean square* (RMS) difference between the estimated TACs and the ground truth TACs used to generate the dynamic projections:

$$RMS\left(TAC_j\right)=\sqrt{\sum_t ¿¿¿¿¿} \quad . \tag{9}$$

2.2.5. CPU time of the main algorithm's iterations is also measured as a function of iteration for comparing SIFADS against pure FADS.

2.3. Data Description: Simulation, Canine, and Human Subject Studies

Simulation. The simulated dynamic datasets were generated from a 64×64×41 array of voxels of an XCAT phantom[48] with a parameter set characteristic for cardiac scans performed using the GE Millennium VG3 Hawkeye SPECT/CT camera (the camera that has been used to acquire human and animal subject data addressed in this paper). The dynamic projections were generated by forward projecting the phantom with presumed tracer activities of ^{99m}Tc-sestamibi over different J tissue-types segmented from the XCAT phantom: left-ventricular blood-pool, myocardial tissue, and liver. Fig 2a shows the TACs used to model the tracer concentration for these three segments of the phantom, respectively, and the corresponding phantom segments in the same colors in Fig 2b, to produce the dynamic projections (some sample slices shown in Fig 3c).

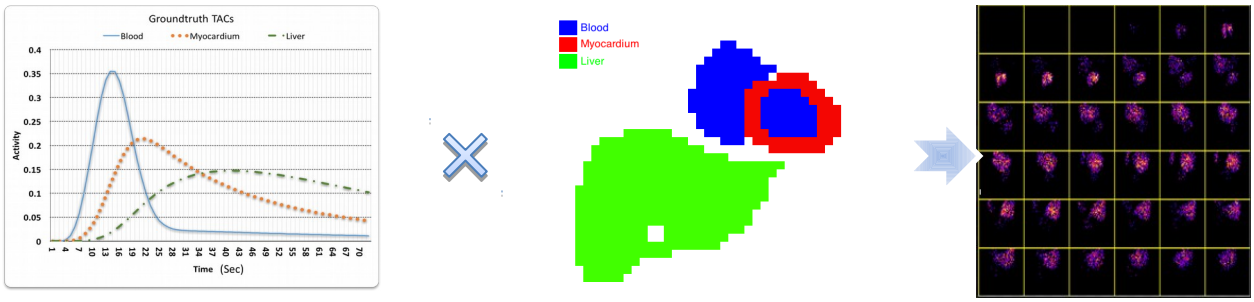

a ***b*** ***c***

Figure 2. Left (***a***), an example of the ground truth TACs and center, segments of XCAT in color, respectively for each curve. Each curve represents how each corresponding segment's intensity is varied while producing the forward projected dynamic data. Middle (***b***), three respective segments of the phantom. Right (***c***), generated dynamic projections with added Poisson noise.

The three curves are based on our expected ideal shape of tracer dynamics as observed before in dynamic SPECT imaging studies[4] and are represented here with b-splines. We use only three segments in this study as our work is focused on heart imaging with SPECT. During simulation the heart was presumed stationary. All the tracers used in this work have very similar dynamics. These segments and the three curves were subsequently used as the ground truth for comparisons with the reconstructed TACs and coefficient images. Poisson noise was subsequently applied to the simulated projection data. Projection data was created using real system matrix of our camera, similar to the one used in animal and human data acquisition. Acquisition parameters used for the forward projection were: (1) LEHR parallel-hole collimation, (2) single head detector, (3) 64×64 bins per projection angle, (4) 72 projections over 360° rotation, and (5) camera rotating at a speed of one second per projection, i.e., 72 seconds for a full rotation.

Canine imaging. The pre-clinical cardiac data set used in this work came from a canine rest-study performed with a GE Millennium VG3 Hawkeye SPECT/CT camera with LEHR parallel-hole collimators where two detector heads were in H-mode (opposite to each other) and rotating continuously. A bolus injection of 3.7 mCi (1.37×10^8 Bq) of ^{201}Tl tracer was administered at the onset of acquisition that continued for 20 minutes. For each rotation, two sets of 72 one-second projections over 360° were acquired. First few rotations (results for 72 seconds for one rotation are shown later) of inconsistent data was used for dynamic reconstruction. However, subsequent projections from consistent data set are used for a static reconstruction that is used inside the dynamic reconstruction algorithm as anatomical prior. Each view contained 64×64 projection bins with 4.42×4.42 mm bin size, close to the intrinsic resolution of the camera.

Human dynamic cardiac data came from a rest study of a standard clinical rest-stress study on a SPECT/CT camera (Infinia Hawkeye 4, GE Healthcare) configured in H-mode (two detectors oriented 180° to each other. Dynamic acquisition began immediately prior to the patient receiving an IV bolus injection (10-20 second

duration) of approximately 10 mCi of 99mTc-tetrofosmin[34]. Two views with a 3° increment every second and a total of 120 projection images (60 views from each camera head) per minute were acquired. The rotation speed of each camera head was 2 minutes per rotation. Projection data were binned into 128×128 detector bins with a bin size of 4.42×4.42 mm. In this work, the projections were cropped to 128×40 pixels (around the heart) to reduce the data size. Projections used in this study is similar to that in canine study mentioned above – first few rotations for dynamic study supported by static reconstruction from consistent projection data.

3. RESULTS

3.1 Simulation Study: Comparison with XCAT data

Fig. 3 shows an example of a comparison of the TACs and the coefficient images obtained using the two algorithms, SIFADS and pure FADS, against the ground truth. A better recoverability of the TACs using SIFADS is clear. When comparing the FADS part of the SIFADS algorithm against the pure FADS (that is, using factor analysis with spline-based pre-initialization versus initialization with arbitrary b-splines), the curves illustrate that, with TACs and coefficients estimated with the spline-based part, the subsequent FADS portion of *SIFADS algorithm is better initialized and the resulting convergence is faster and better (as observed from resulting coefficient images, TACs, and often with the convergence parameters) than the pure FADS*.

We ran the SIFADS and FADS algorithms several times with different initializing b-splines, and each time both algorithms started with the same set of b-splines. Each column of Fig. 4 corresponds to each initializing b-spline set presented in the first row. For each of the three initializing splines the SIFADS algorithm demonstrates faster convergence and better optimization than the pure FADS algorithm. Fig. 4 shows measures of convergence for the two algorithms versus iteration for three different initializing b-splines. The figure shows the convergence (eq. 8), the estimation error (eq. 3), and the value of the a-posterior function (eq. 4) versus iteration in rows Figs 4d-f, Figs 3g-i, and Figs 4j-l, respectively.

SIFADS has two phases of iterative processes: spline-based optimization and then FADS optimization. We distinguish between these two types of iterations as *pure spline-based iterations* and *FADS-iterations*. FADS algorithm has only FADS-

iterations. We compared the performance of the two algorithms for thirty-five iterations. Two FADS-iterations take approximately the same time as five pure spline-based iterations used within SIFADS (see table 1 below). Hence, we adjust for the overhead pre-initialization time of SIFADS (blue curve) with two units on each plot’s x-axis toward the right. Note that the pure spline-based optimization algorithm optimizes only for the coefficients of the splines, wheras the FADS algorithm optimizes for both the factors (starting with the splines) and their coefficients[1], and hence, a FADS iteration takes more time than a spline-based one.

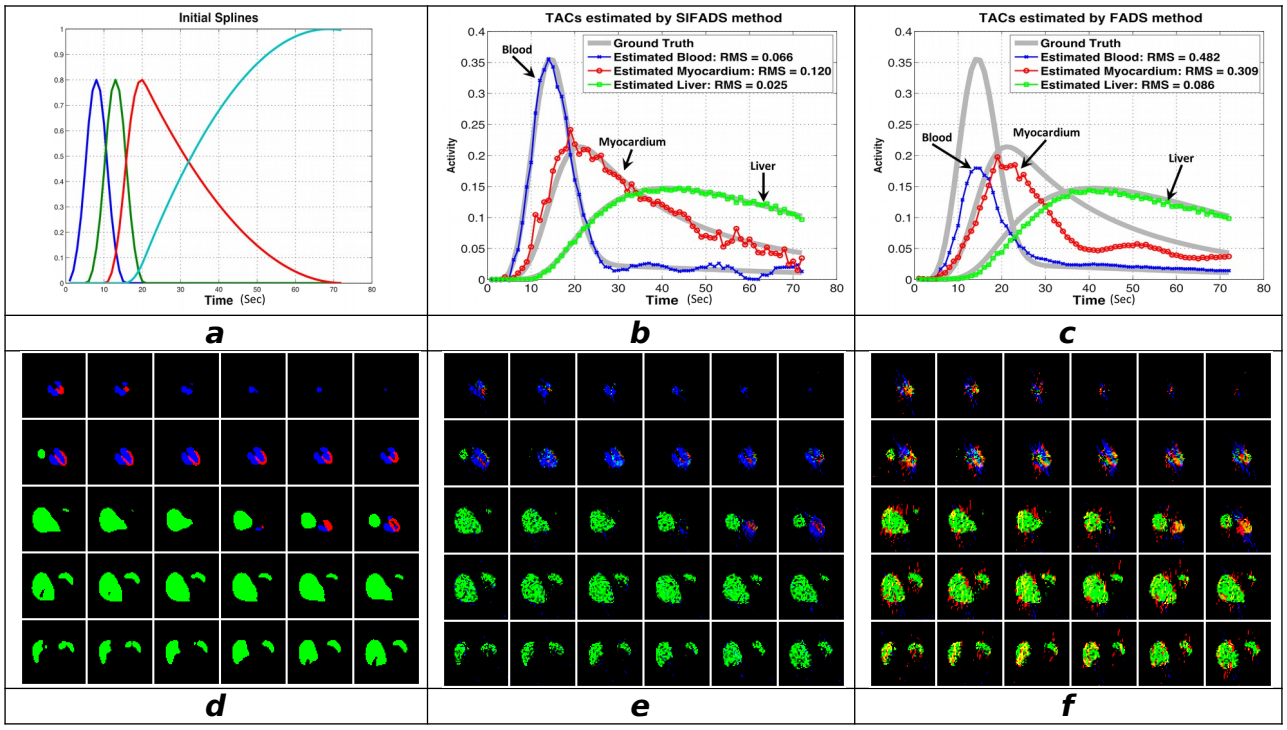

Figure 3. *Results of SIFADS and FADS algorithms using simulation data*. ***a***: the spline functions used in both algorithms for initialization. ***b***: ground truth TACs (grey background curve) along with resulting TACs after 30 iterations using SIFADS, and ***c:*** the same result using FADS. SIFADS produces better TACs. 2nd row: ***d:*** ground truth coefficients, ***e:*** resulting coefficients from SIFADS, and ***f:*** those from FADS (right col.). Activity values on resulting TACs (y-axis) and intensity values on voxels of coefficients are relative. TAC values are relative to that of input initial spline, where the peak value is 1 (for the fourth open spline on ***a***) and coefficient voxel values are in terms of gamma counts in sinogram, such that TACs multiplied with coefficient values of respective voxels (eq. 2) produces the respective estimated gamma counts on voxels on resulting 4D image.

Fig 4 shows that SIFADS and FADS converge to similar values given enough time. However, SIFADS produces better estimation in less time (i.e., with less iterations), even including the extra overhead for the iterations in the spline-based initialization. For example, only five iterations of SIFADS will produce better results than FADS with seven iterations with arbitrary initialization (two FADS-iterations take equivalent time to that of five spline-based pre-initialization steps within SIFADS). We chose 35 iterations because we did not see much change in the updates of the images as our measures of convergence demonstrate. Achieving full convergence is very time consuming.

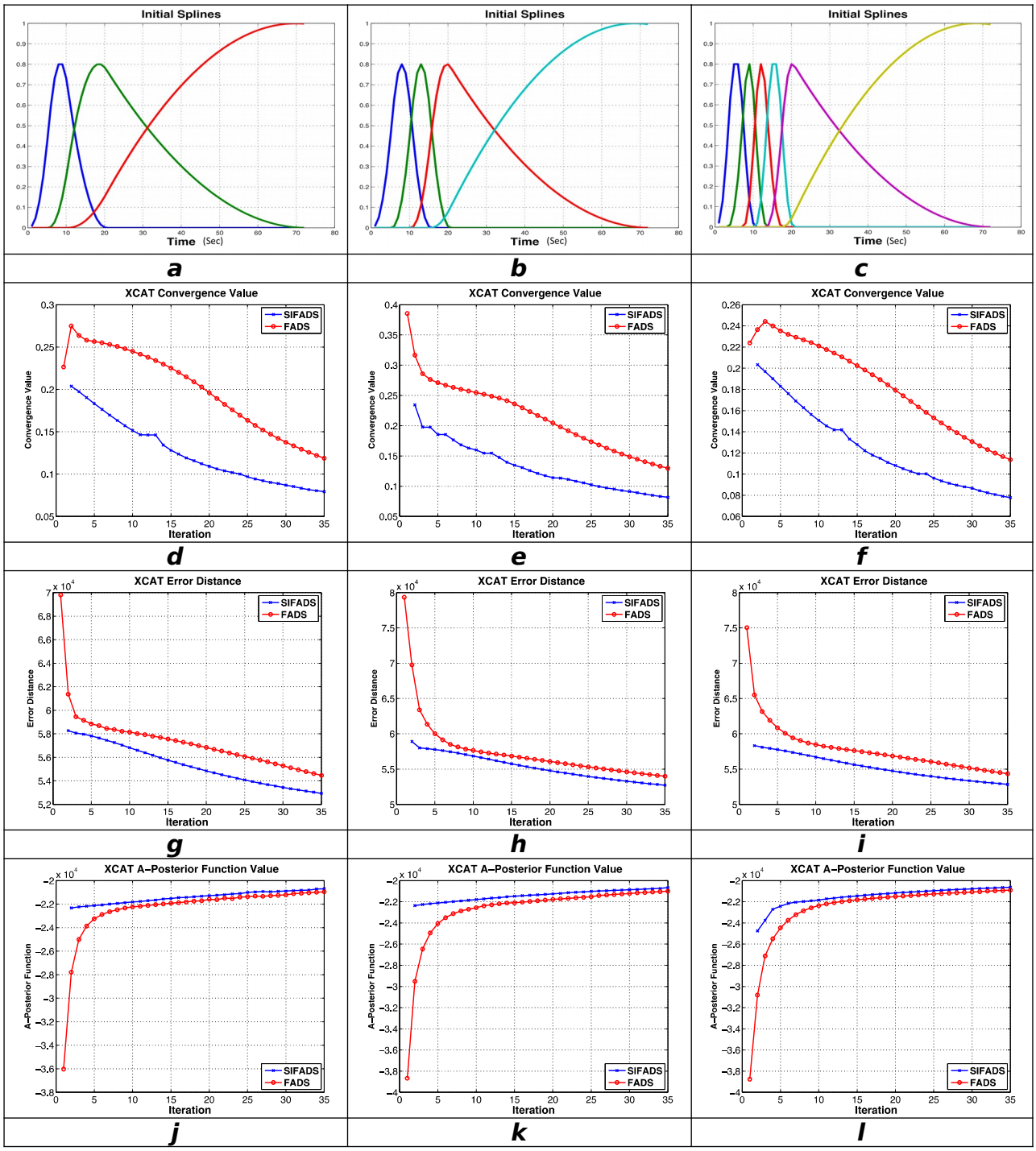

Figure 4. *Results of comparison measures using the simulation data.* 1st row of each column (***a-c***): three different initializing b-splines. 2nd row (***d-f***): convergence values (eq. 8); 3rd row (***g-i***): error distance (eq. 3); 4th row (***j-l***): a-posteriori functional values (eq. 4) versus number of iterations. The SIFADS curves (blue) are artificially shifted here by 2 iterations on x-axis to compensate for the spline-initialization overhead time. Contrast of convergence between the two algorithms is mostly observed between 5 to 10 iterations. We show results for up to 35 iterations on x-axis.

Fig 5 shows the resulting curves in respective columns for the same initializing b-splines as in Figs 4a-c first row. Figs 5a-c shows the corresponding results for arbitrary initialized FADS, and Figs 5d-f shows the same with SIFADS.

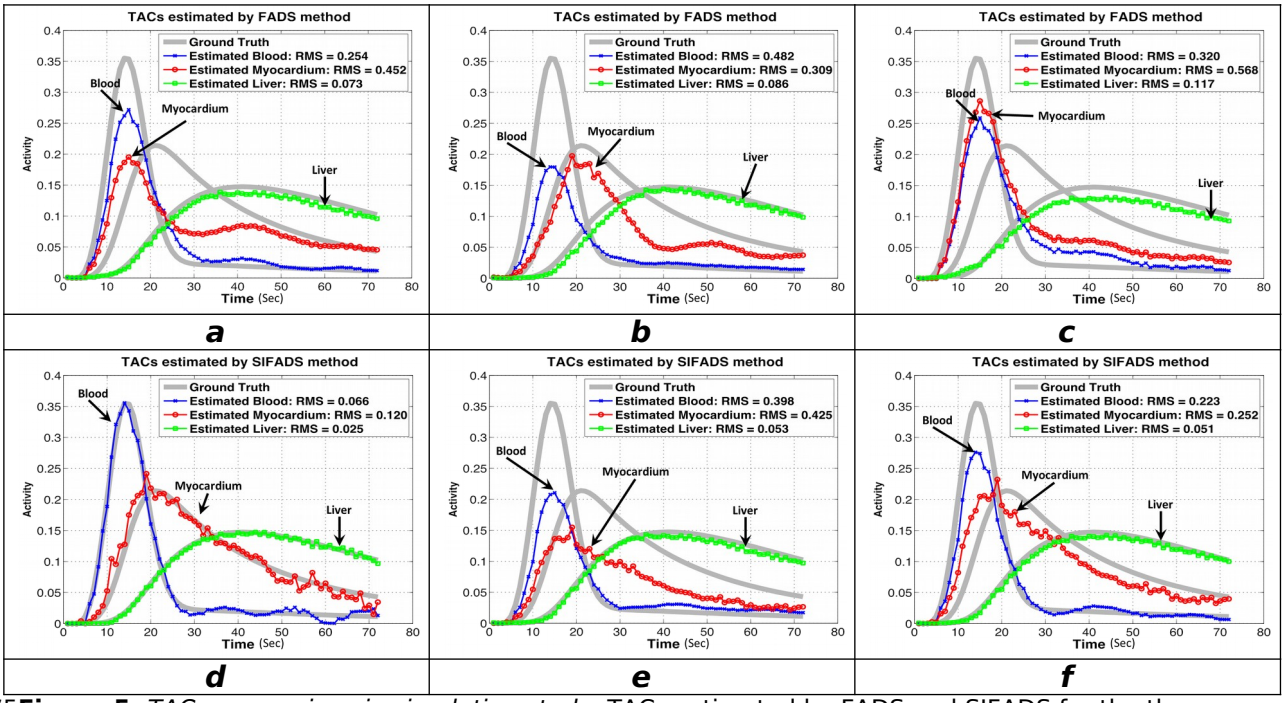

Figure 5. *TACs comparison in simulation study.* TACs estimated by FADS and SIFADS for the three initializations as in Fig. 4. 1st row (***a-c***): TACs estimated by the FADS algorithm. 2nd row (***d-f***): TACs estimated by the SIFADS algorithm. Ground truth curves are shown in grey for comparison. Lesser RMS values for each curve in plots show that SIFADS consistently produces better curves.

Table 1 has the computation times for the FADS and SIFADS algorithms. All algorithms were implemented and evaluated on an Apple Xserve (Early 2009 version) running Mac OS X server. The machine had two dual quad-core 2.93 GHz Xeon processors and 12 GB of RAM. We report below the timings for SIFADS in two parts: spline-based pre-initialization and FADS (first row, columns 3 and 4). Timings for pure FADS are in the second row.

3.2. Canine Study

Fig. 6 shows estimated TACs from the canine SPECT study. Even though the curves exhibit significant mutual contamination between tissues, SIFADS-computed factors describe the expected physiology of the LV blood pool concentration more realistically. Also, the reconstructed coefficient images computed with SIFADS (Fig. 7a and c) demonstrate better separation between different tissue types, whereas the coefficients estimated by FADS with

393 blind initialization (Fig. 7b and d) are much more smeared between different tissue types. All
394 relevant results including 3D images are available online for any interested reader to view[48].
395

	Convergence Value (Eq. 8)	***Computing time of initial Coefficients and TACs with spline-method (sec)***	***FADS time (sec)***	***Total time (sec)***	***Error Distance of Last Iteration (Eq. 3)***	***RMS of TACs (Eq. 9)***
SIFADS CPU (5 spline-based iterations, and subsequent 30 FADS-iterations)	0.172	44.931 (5 iterations) 8.99 /iterations	390.632 13 /FADS-iterations	435.5 63	0.285	0.070
Pure FADS (30 FADS-iterations)	0.179	-	507.031 16.90 /FADS-iterations	507.0 31	0.285	0.292

Table 1. *Computation times* for the FADS and SIFADS algorithms in processing the simulated data. The spline-based initialization phase in the SIFADS algorithm can accelerate the conventional FADS algorithm in spite of the fact that it needs more time to prepare the initial TACs and coefficients. These results are from the first initialization in column 1 of Fig. 5.

Fig. 8 shows comparisons of the SIFADS and pure FADS algorithms in terms of rates of convergence, image quality, and the a-posterior function values versus iteration for the canine data set. Note that although the number of initializing spline-curves for SIFADS may differ (in each of our experiments as shown in Figs 8a-c) the number of factors are determined by the number of segments we want to extract from the data, determined by visual inspection of the projections data (or by trial and error, or by the targeted diagnostic application). Surprisingly, the projection error

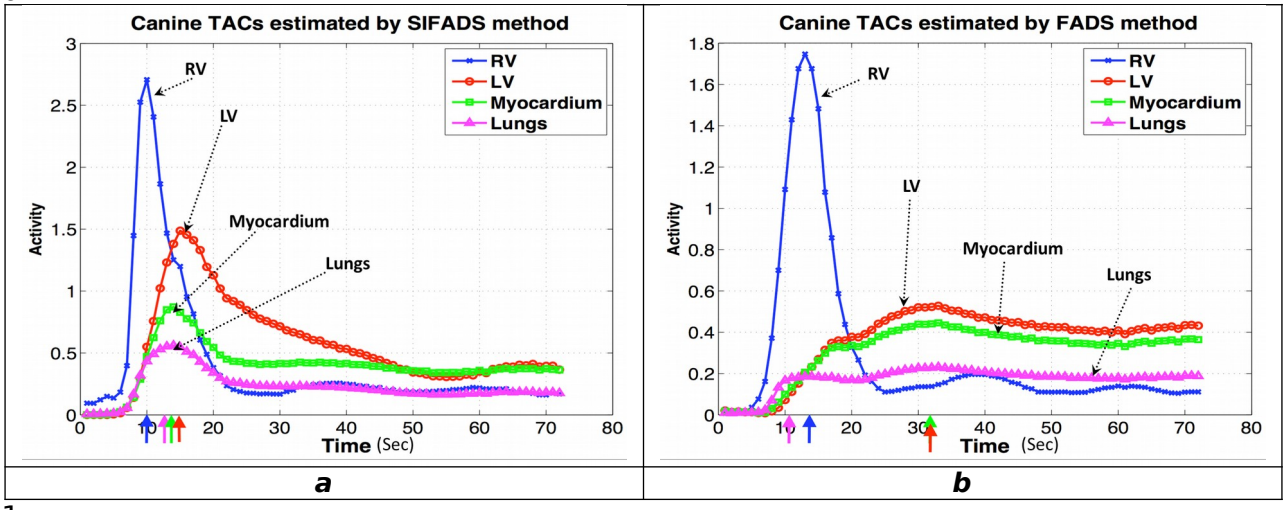

Figure 6. *Estimated TACs for the canine SPECT study* by: (***a***) SIFADS and (***b***) FADS. The arrows on the x-axis show the time at which the tracer uptake arrives to a peak: RV first (blue), then myocardium

(green) followed by (or simultaneously with) LV (red). Lungs (purple) peak appears at relatively different times for the two algorithms

and the value of the *a-posterior* function do not differ significantly at large number of iterations, suggesting fewer iterations are sufficient. FADS shows better or very similar convergence characteristics for the first two criteria, whereas SIFADS shows better a-posterior convergence when initial curves are widely different from expected final curves (last two columns of Fig. 8). Fluctuations of the metrics observed for both algorithms are for reasons unknown to us, but they do not affect the overall observations. Possibly, they are related to the removal and reintroduction of zero values on coefficients as iteration progresses. This is because our implementation avoids storing and computing lower-than-threshold values that we consider as zero's.

Corresponding to the initialized b-splines of Figs 8a-c, the resulting TACs for pure FADS and SIFADS are shown in the two rows of Fig 9, respectively. SIFADS-computed TACs describe the expected physiological timing of the RV and LV blood pool concentrations, and lung and myocardial tissue concentrations more realistic.

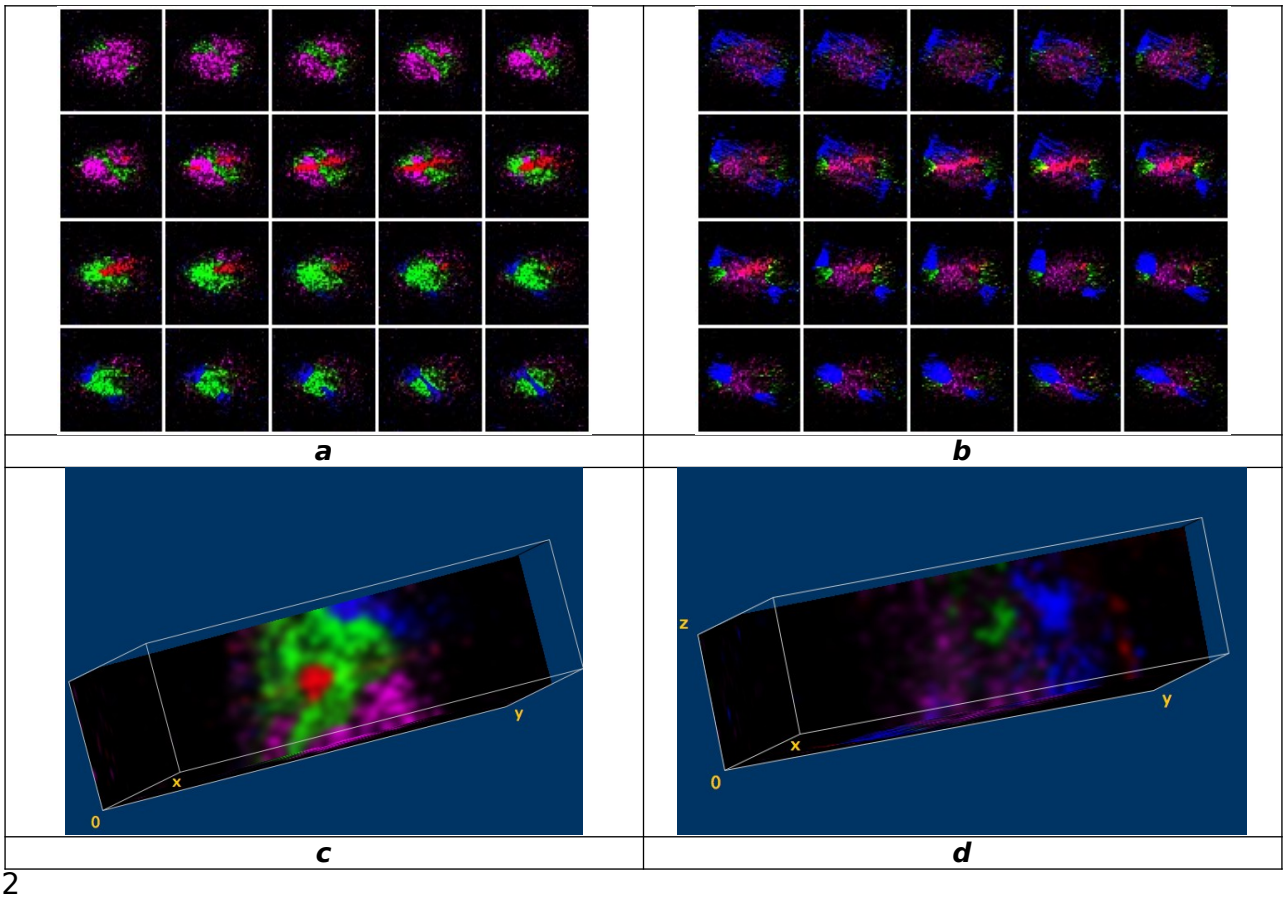

433**Figure 7.** *Estimated tissue coefficient images for the canine SPECT study* by: (***a*** and ***c***) SIFADS, and (***b***
434and ***d***) FADS. The upper row (**a** and **b**) shows some slices of respective coefficients and the lower row
435(***c*** and ***d***) shows the same images in 3D from SIFADS and FADS respectively.
436

437

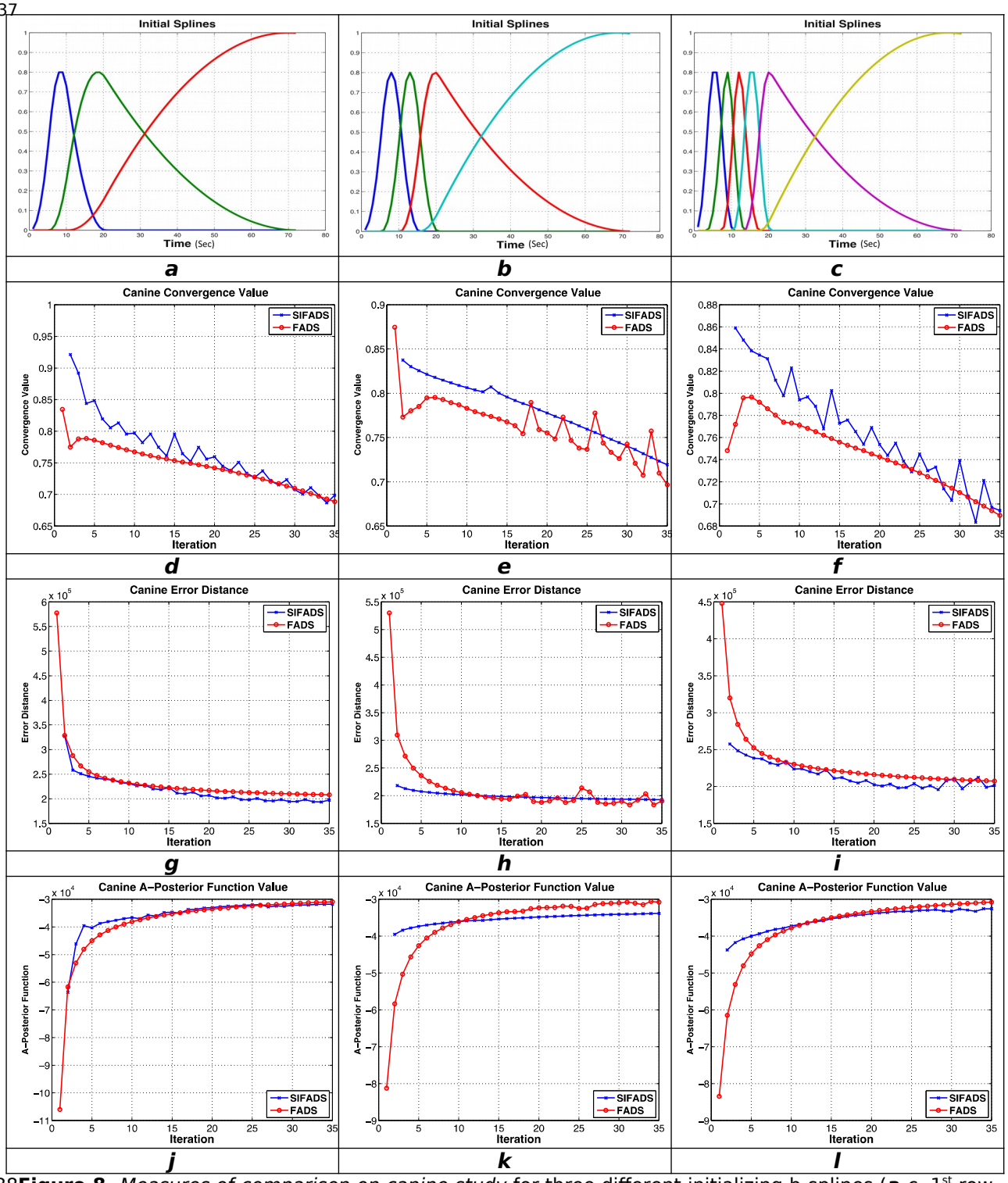

438**Figure 8.** *Measures of comparison on canine study* for three different initializing b-splines (***a-***c, 1st row 439for each column). 2nd row (***d-f***): convergence values (eq. 8); 3rd row (***g-i***): error distance (eq. 3); 4th row 440(***j-l***): a-posteriori functional value (eq. 4) all versus number of iterations. The resulting SIFADS curves 441(blue) are shifted by 1 iteration to compensate for the overhead time in the spline initialization (see 442table 2 below).

443

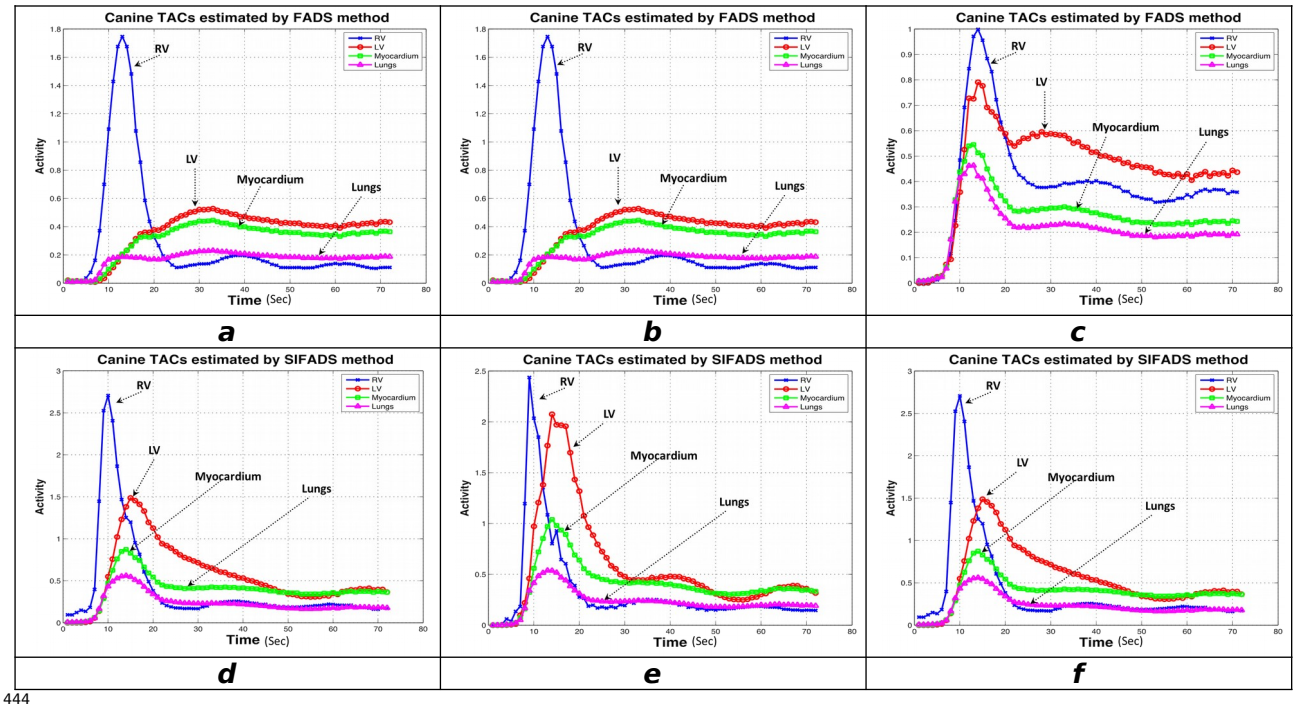

Figure 9. *Estimated TACs* by FADS and SIFADS for the three initializations in Fig. 8. 1st row (***a-c***): TACs estimated by the FADS algorithm. 2nd row (***d-f***): TACs estimated by the SIFADS algorithm. Blue curves for RV, red curves for LV, green curves for myocardium and purple curves for lungs.

Table 2 shows that SIFADS exhibits only minor reduction in time per iteration compared to pure FADS. We believe the speed up becomes less as the data becomes more complex and noisy. This happens because fewer non-zero values are obtained in the intermediate results as our implementation ignores only zero values. There is no ground truth for the TACs for the real data to measure the RMS error value, as was for the simulation data in table 1.

	Convergence Value (Eq. 8)	***Computing time of initial Coefficients and TACs with spline-method (sec)***	***FADS time (sec)***	***Total time (sec)***	***Error Distance on Last Iteration (Eq. 3)***
SIFADS CPU (5 spline-based iterations, and 30 subsequent FADS-iterations)	1.674566	56.293 (*5 iterations*) 11.25 /iterations	486.794 16.06 /FADS-iterations	543.087	2.5043
Pure FADS (30 FADS-iterations)	1.793	-	488.049 16.27 /FADS-iterations	488.049	2.852

Table 2. *Computation times* for the FADS and SIFADS algorithms in processing the *canine* data. Convergence value and running time for the two methods in estimating TACs from the canine data with 30 iterations. These results are from the first initialization in column 1 of Fig. 8.

3.3. Human Study

Fig 10 shows the same set of comparisons as in the previous studies with the two algorithms used to estimate TACs from data in a human dynamic SPECT study. At a first glance, the TACs from pure FADS in Fig 10b appear to separate RV and LV TACs as can be seen in Fig 9. However, visually on Fig 10a, SIFADS provides better overall tissue separation.

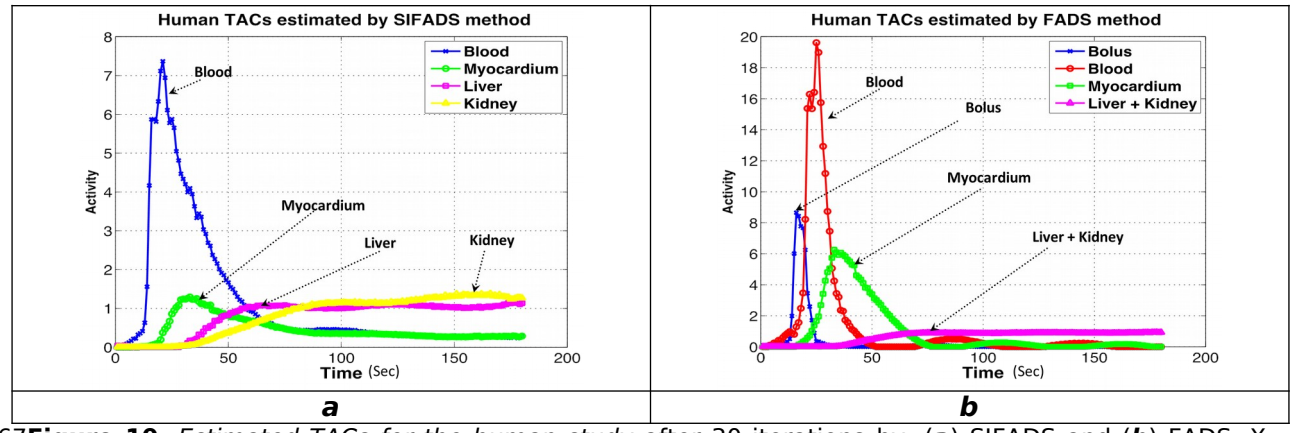

Figure 10. *Estimated TACs for the human study* after 30 iterations by: (***a***) SIFADS and (***b***) FADS. X-axis in time in seconds. Blue curves for RV, red curves for LV, green curves for myocardium and purple curves for lungs.

SIFADS estimates the blood tracer concentration as a single curve (blue in Fig. 10). The myocardium seems to be well represented by the green curve (see its coefficients in Fig. 11 below where it shows a clear shape of the heart). On the other hand, FADS (right) estimates two curves for blood (blue for RV and red for LV). However, the RV curve (blue) has a lower signal than the LV (red), which is unrealistic and not obvious in the projection data. Also, the myocardium curve (green) seems to have an unrealistically fast uptake and washout (50 sec). Furthermore, liver and kidney TACs are mixed together in the FADS results. Each frame in Fig. 11 consists of an overlay of the corresponding four color-coded slices from the four 3D coefficient images, where the colors are the same as that for the corresponding curves of factors in Fig. 10. It is evident by the coefficients of SIFADS that the tissue types are better distinguishable (each color represents a tissue type, i.e., blood, heart, liver, or kidneys). This is in contrast to the fact that the coefficients estimated by FADS are not well separated.

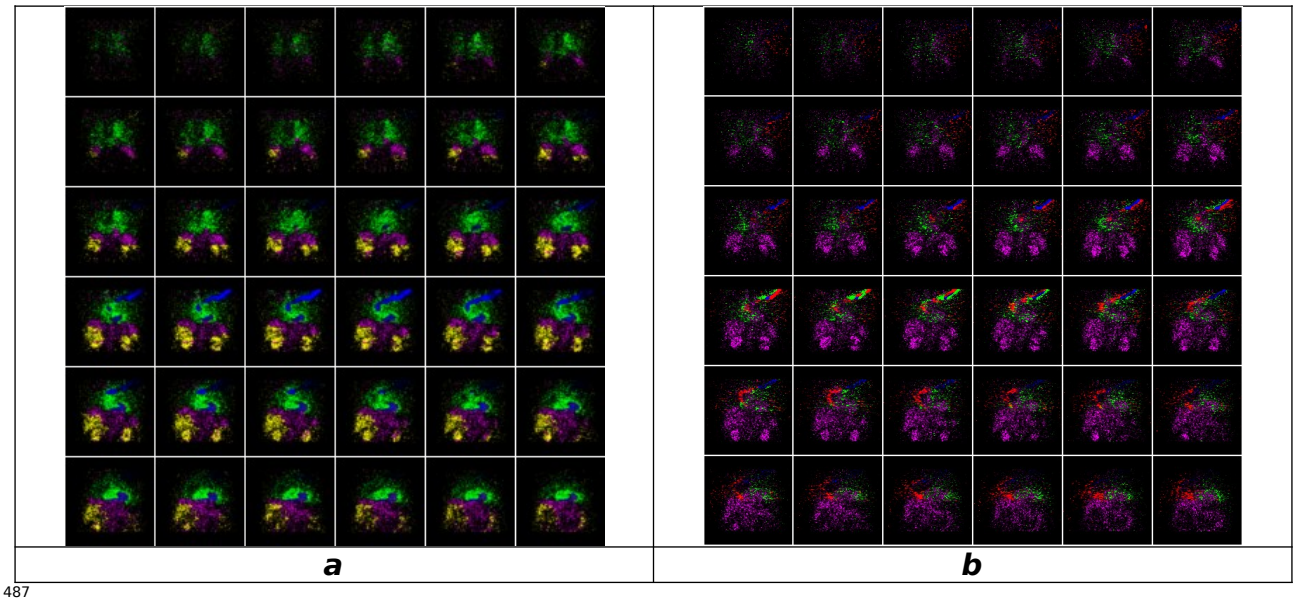

Figure 11. *Coefficient images.* Frames from color-coded superimposed coefficient images after 30 iterations of SIFADS (***a***) and pure FADS (***b***). Colors are assigned based on the corresponding TACs' colors as in Fig. 10: Blue for RV, red for LV, green for myocardium and purple for lungs.

We believe that the FADS curves are less accurate because: 1) LV actually has a stronger signal than the RV (as seen in the projections) as opposed to what the pure FADS curve is showing. 2) Coefficients from pure FADS visually do not show the clear segmentation observable in the SIFADS coefficient images. Visual inspection of the coefficients obtained from pure FADS does not allow clear correspondence of the blue and red curves to specific ventricular regions whereas in SIFADS the unseparated blue curve clearly corresponds to a single ventricular region. 3) Liver is not clearly segmented with pure FADS despite being well defined in the projections.

501

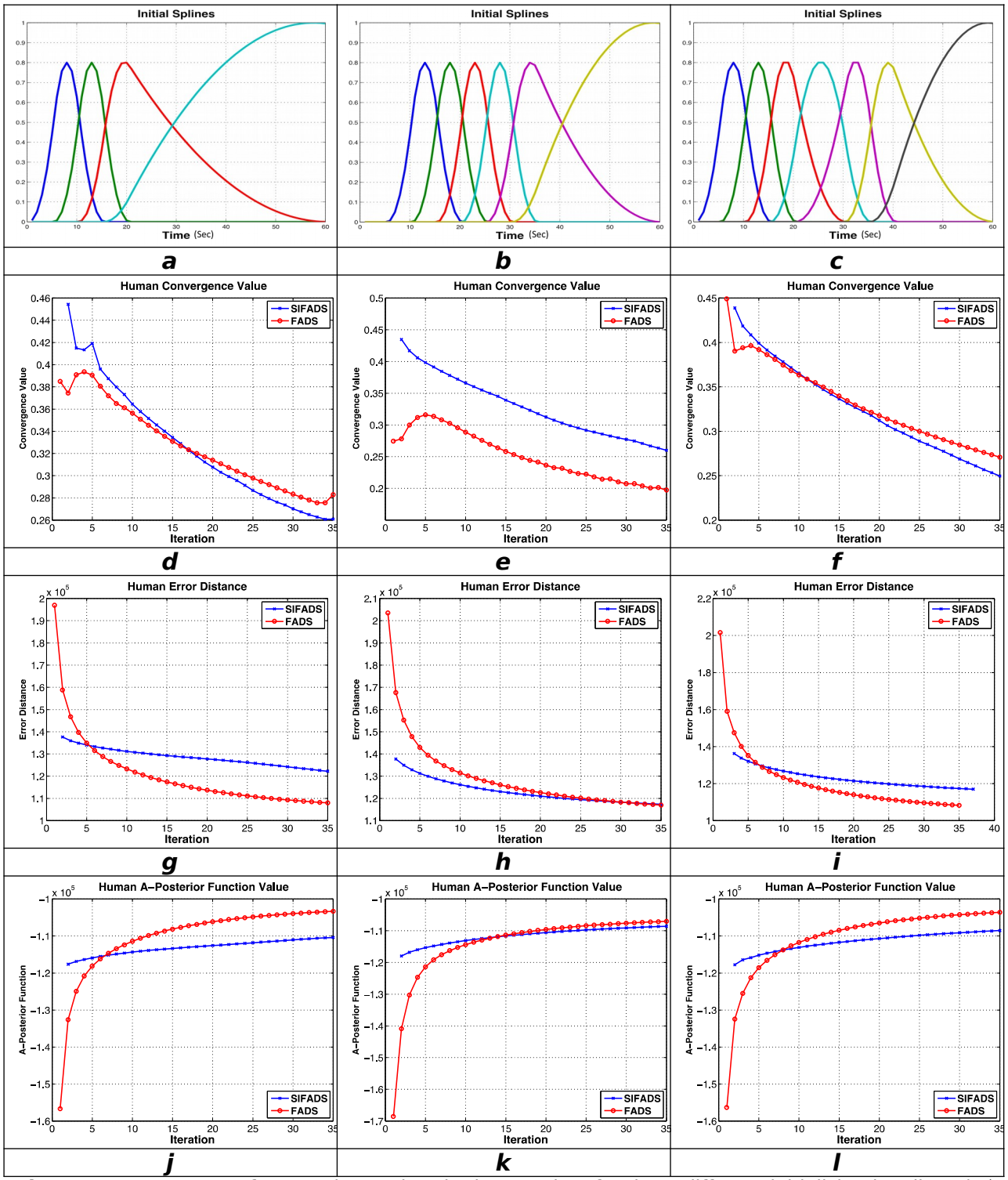

502**Figure 12.** *Measures of comparison using the human data* for three different initializing b-splines (1st
503row for each column, ***a-c***). 2nd row (***d-f***): convergence values (eq. 8); 3rd row (***g-i***): error distance (eq.
5043); 4th row (***j-l***): a-posteriori functional values (eq. 4) versus number of iterations. The SIFADS curves
505(blue) are shifted by 1 iteration to compensate for the spline-initialization overhead time (see table 3).
506Blue curves for RV, red curves for LV, green curves for myocardium and purple curves for lungs.

507

Fig 12a-c shows three sets of initial b-splines, and the subsequent rows display the algorithm performance measures corresponding to these sets. All three performance measures for SIFADS (blue curves) are notably similar across the three initialization sets, demonstrating the stability and reproducibility of the algorithm. Convergence plots in Fig 12d-f show that in two cases (first and third columns, Figs 12d and f) SIFADS achieves better convergence than pure FADS after a few iterations. The third row Figs 12g-i present error distances (eq. 3) between the estimated and the actual projections indicates that pure FADS better estimates the projections. The human scan data were extremely noisy, and SIFADS actually removed more noise than did FADS, thus, the solution deviated further from the input data. The a-posteriori function values in the fourth row Figs 12j-l suggest that FADS outperforms SIFADS after 6 to 12 iterations. This is an anomalous result since the optimization in both algorithms is performed with the same objective function, and we clearly see better segmentation in the coefficient images produced by SIFADS after thirty iterations (see Fig. 11 and the data available on the provided link[48]). This may mean that SIFADS and FADS are converging to two different local minima and the local minimum attained by SIFADS is better suited for the purpose of tissue segmentation based on tracer kinetics.

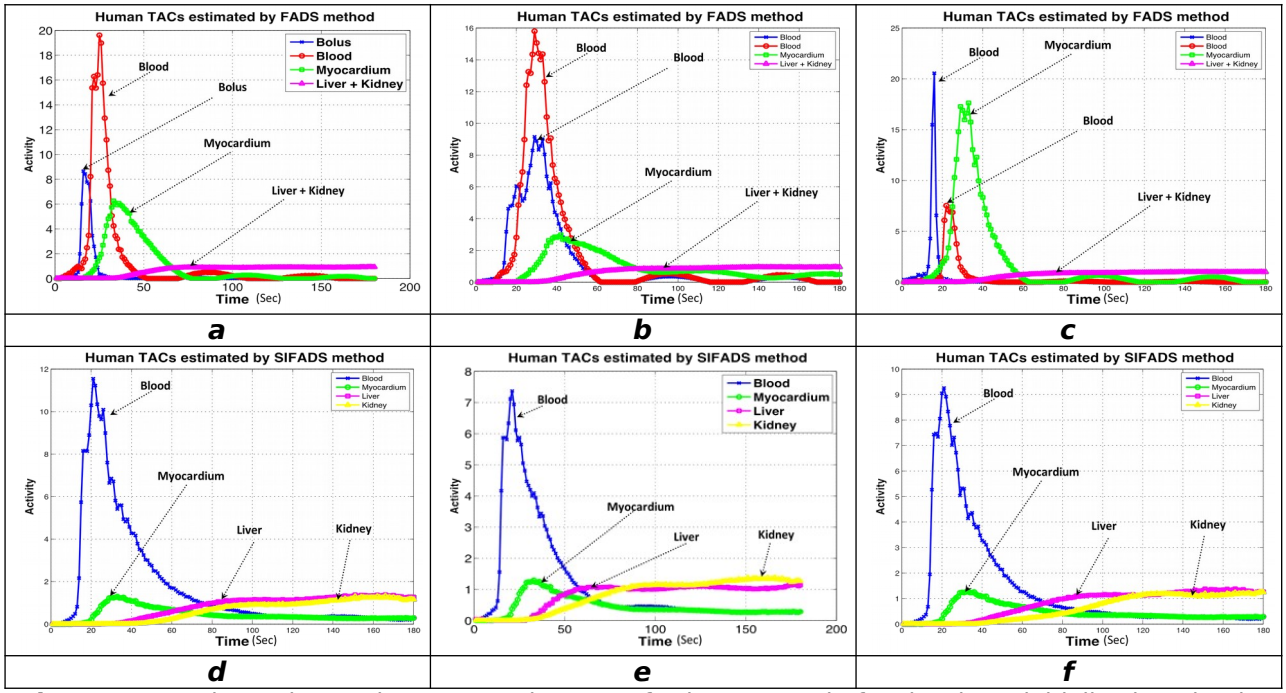

Figure 13. *Estimated TACs by FADS and SIFADS for human study* for the three initializations in Fig. 12. 1st row (***a-c***): TACs estimated by the FADS algorithm. 2nd row (***d-f***): TACs estimated by the SIFADS algorithm. Blue curves for RV, red curves for LV, green curves for myocardium and purple curves for lungs.

TACs computed from two algorithms corresponding to different initializations (Fig. 12, first row) are shown in the two rows of Fig. 13, respectively. SIFADS-computed TACs describe the expected physiology more realistically.

533

	Convergence Value (Eq. 8)	Computing time of initial Coefficients and TACs with spline-method (sec)	FADS time (sec)	Total time (sec)	Error Distance at Last Iteration (Eq. 3)
SIFADS (5 spline-based iterations, and 30 FADS-iterations)	0.54	2444.21 (*5 iterations*) 488.84 sec / iterations	22961.86 765.40 sec / FADS-iterations	25406.07	0.37
FADS (30 iterations)	1.30	-	22633.06 754.44 Sec / FADS-iterations	22633.06	0.39

Table 3. *Computation times* for the FADS and SIFADS algorithms in processing the human data. Convergence values and run times for the three methods in reconstructing the TACs from the human data. These results are from the first initialization in column 1 of Fig. 12.

Table 3 shows that the pure FADS algorithm surprisingly takes slightly less time per iteration on average for the human data although its convergence is slower (Figs 12d-f, and table 3-column 1).

4. Discussion

The focus of this paper was to compare accuracy and convergence properties of SIFADS and FADS reconstruction algorithms. SIFADS clearly performs better on all three performance measures for simulated data, reconstructing dynamic noise-added data generated from the XCAT phantom (Figs 3-5). This was true for any number of iterations. In the canine study (Fig 8), although FADS attains better values for the a-posterior objective function after around ten iterations, the physiological features estimated by SIFADS is more realistic (Fig 7). For the human study (Fig 12), the objective function values for the two algorithms cross-over between 8 to 15 iterations, depending on the initialization. The other two measures of convergence and error distance seem to follow fairly similar trends after a few iterations, again depending on the initialization. Overall, SIFADS seems to provide better estimates of the expected physiological aspects of the tracer kinetics with fewer iterations (only 5) than FADS. Note that the curves estimated by SIFADS are already adjusted for the overhead time to determine the initial spline coefficients.

We believe that SIFADS and FADS are converging to different local minima because of different initializations. Even though FADS shows different values of the objective function than that of SIFADS after 30 iterations (human data, Fig 9) the estimated

TACs and coefficient images with SIFADS appear much more realistic upon visual inspection as shown in Figs. 10-11[48], over a range of iterations. This observation leads us to conjecture that the a-posterior objective function is not the best performance metric for estimating the quality of segmenting tissue based on the tracer dynamics.

In the previous section, we commented that the FADS iterations take less computation time as opposed to those of SIFADS (table 3, third column). This seemingly counter-intuitive effect is explained by the procedure of how zero values are eliminated below a pre-assigned threshold from being processed further in the reconstruction. Some factor values approach zero after only a few FADS iterations. Potentially, this may compromise the estimation of TACs by pure FADS by providing less realistic TACs in return for slight improvement in efficiency.

One may observe in the plots in Figs 6, 9 and 13 that many curves are converging to similar values and thus wonder why then one sees clear segmentations for a static reconstruction with the same tracer. The reason for this is the fact that the intensity values in static and dynamic imaging have different interpretation. The sestamibi uptake in the heart begins immediately with the injection and continues with little washout. At the start of the static perfusion study approximately 60-70 mins later there is excellent contrast between the myocardium and the blood in the left ventricular cavity. The plots show that at that time there is very little activity in the blood in the left ventricular cavity; whereas, the activity in the heart is the integral of the time activity curve shown here for the heart over the 60-70 minutes. This integral of activity provides excellent contrast compared with the background blood activity.

5. Conclusion

FADS is a powerful method capable of reconstructing tissue TACs and spatial distributions from dynamic SPECT projections; however, it is overly sensitive to the initialization both in terms of performance and the reconstruction accuracy. FADS accuracy and convergence time may be improved by using b-spline-based initialization of the factors implemented in our SIFADS algorithm. SIFADS clearly

outperforms FADS in reconstruction of simulated phantom study as seen from our results presented here. However, in order to check its performance further on real data we have compared SIFADS with FADS on data sets of canine and human studies. When reconstructing on these real data, numerical performance comparisons do not give clear advantage to either algorithm, however, the tissue distribution images obtained with SIFADS appear to be more physiologically meaningful. This suggests a few primary directions for future work: (1) Changing the objective function formulation that reflects our goal of tracer-dynamics based segmentation may further improve the quality of the dynamic SPECT reconstruction. (2) Alternative initialization techniques (other than the spline-based one as in SIFADS) may be explored[2] to address the non-uniqueness of FADS. (3) How cardiac motions affects the dynamics needs to be studied[39] with respect our initialization techniques.

All real data sets used here were acquired on past projects with appropriate Institutional Review Board's and animal care and use committee's approvals at Lawrence Berkeley National Laboratory, California.

5. Acknowledgements

This work was supported by National Institute of Health grant numbers R01EB07219, R01HL50663, R01HL135490 and R01CA154561.

References:

1. Abdalah M, Boutchko R, Mitra D and Gullberg GT. Reconstruction of 4-D Dynamic SPECT Images from inconsistent projections using a spline initialized FADS algorithm (SIFADS). *IEEE Trans Med Imaging.* 2015;34(1):216-228.
2. Boutchko R, Mitra D, Baker SL, Jagust WJ, and Gullberg GT. Clustering-initiated factor analysis application for tissue classification in dynamic brain positron emission tomography. *Jnl. Cerebral Blood Flow & Metabolism*, 1–8. 2015;35(7):1104-1111. doi:10.1038/jcbfm.
3. Seung HS, and Lee DD. Learning the parts of objects by non-negative factorization. *Nature*. 1999;401 (6755):788-791.

4. Sitek A, Di Bella EV and Gullberg GT. Factor Analysis with a priori knowledge application in dynamic cardiac SPECT. *Phys. Med. Biol*. 2000;45(9):2619-2638.

5. Sitek A, Di Bella EVR, Gullberg GT, Huesman RH. Removal of liver activity contamination in teboroxime dynamic cardiac SPECT imaging using factor analysis. *J Nucl Cardiol.* 2002;9(2):197-205.

6. Farncombe T, Celler A, Noll D, Maeght J and Harrop R. Dynamic SPECT imaging using a single camera rotation (dSPECT). *IEEE Trans Nucl Sci*. 1999;46(4): 1055-1061.

7. Celler A, Farncombe T, Bever C, et al. Performance of the dynamic single photon emission computed tomography (dSPECT) method for decreasing or increasing activity changes. *Phys Med Biol.* 2000:45(12):3525-3543.

8. Hsu B, Chen FC, Wu TC, et al. Quantitation of myocardial blood flow and myocardial flow reserve with ^{99m}Tc-sestamibi dynamic SPECT/CT to enhance detection of coronary artery disease. *Europ J Nucl Med and Mol Imag*. 2014;41(12):2294-2306.

9. Shrestha U, Sciammarella M, Alhassen F, et al. Measurement of absolute myocardial blood flow in humans using dynamic cardiac SPECT and ^{99m}Tc-tetrofosmin: Method and validation. *J Nucl Cardiol.* 2014;24(1):268-277.

10. Winant CD, Aparici CM, Zelnik YR, et al. Investigation of dynamic SPECT measurements of the arterial input function in human subjects using simulation, phantom and human studies. *Phys Med Biol.* 2012;57(2):375-93.

11. Ben-Haim S, Murthy VL, Breault C, et al. Quantification of myocardial perfusion reserve using dynamic SPECT imaging in humans: A feasibility study. *J Nucl Med.* 2013;54(6):873-879.

12. Wells RG, Timmins R, Klein R, et al. Dynamic spect measurement of absolute myocardial blood flow in a porcine model. *J Nucl Med*. 2014;55(10):1685- 1691.

13. Ben Bouallègue F, Roubille F, Lattuca B, et al. SPECT myocardial perfusion reserve in patients with multivessel coronary disease: Correlation with angiographic findings and invasive fractional flow reserve measurements. *J Nucl Med*. 2015;56(11):1712-1717.

14. Lau CH, Eberl S, Feng D, et al. Optimized acquisition time and image sampling for dynamic SPECT of Tl-201. *IEEE Trans Med Imag*. 1998;17(3):334-343.

15. Smith AM, Gullberg GT, Datz FL, Christian PE. Kinetic modelling of teboroxime using dynamic SPECT imaging. *J Nucl Med.* 1994;35(3):484-495.

16. Chiao P, Ficaro EP, Dayanikli F, Rogers WL, Schwaiger M. Compartmental analysis of technetium-99m-teboroxime kinetics employing fast dynamic SPECT at rest and stress. *J Nucl Med.* 1994;35(8):1265-1273.

17. Di Bella EVR, Ross SG, Kadrmas DJ, et al. Compartmental modeling of technetium-99m-labeled teboroxime with dynamic single-photon emission computed tomography: Comparison to static thallium-201 in a canine model. *Invest Radiol.* 2001;36(3):178-185.

18. Okada DR, Johnson 3rd G, Okada RD. Myocardial clearance of technetium-99m-teboroxime in reperfused injured canine myocardium. *EJNMMI Research* 2014;4(1):1-9.

19. Klein R, Hung GU, Wu TC, et al. Feasibility and operator variability of myocardial blood flow and reserve measurements with ^{99m}Tc-sestamibi quantitative dynamic SPECT/CT imaging. *J Nucl Cardiol.* 2014;21(6):1075-1088.

20. Alhassen F, Nguyen N, Bains S, et al. Myocardial blood flow measurement with a conventional dual-head SPECT/CT with spatiotemporal iterative reconstructions – A clinical feasibility study. *Am J Nucl Med Mol Imaging.* 2014;4(1):53-59.

21. Sciammarella M, Shrestha UM, Seo Y, Gullberg GT, Botvinick EH. A combined static-dynamic single-dose imaging protocol to compare the quantitative dynamic SPECT with static conventional SPECT [published online ahead of print Aug 3, 2017]. *J Nucl Cardiol.* doi: 10.1007/s12350-017-1016-7.

22. Reutter BW, Gullberg GT, Huesman RH. Direct least squares estimation of spatiotemporal distributions from dynamic SPECT projections using a spatial segmentation and temporal B-splines. *IEEE Trans Med Imaging.* 2000;19(5):434-450.

23. Niu X, Yang Y, Jin M, Wernick MN, King MA. Effects of motion, attenuation, and scatter corrections on gated cardiac SPECT reconstruction. *Med Phys.* 2011;38(12):6571-6584.

24. Hutton BF, Ben-Haim S. What are the necessary corrections for dynamic cardiac SPECT? *J Nucl Cardiol*. 2016;24(4):1347-1349.

25. Wang L, Wu D, Yang Y, et al. Avoiding full corrections in dynamic SPECT images impacts the performance of SPECT myocardial blood flow quantitation. *J Nucl Cardiol.* 2016;24(4):1332-1346.

26. Gullberg, GT, Reutter BW, Sitek A, Maltz J, Budinger TF. Dynamic single photon emission computed tomography – Basic principles and cardiac applications. *Phys Med Biol.* 2010;55(20):111-191.

27. Feng B, Pretorius PH, Farncombe TH, et al. Simultaneous assessment of cardiac perfusion and function using 5-dimensional imaging with Tc-99m teboroxime. *J Nucl Cardiol.* 2006;13(3):354-361.

28. Jin M, Yang Y, King MA. Reconstruction of dynamic gated cardiac SPECT. *Med Phys.* 2006;33(11):4384-4394.

29. Shrestha UM, Seo Y, Botvinick EH, Gullberg GT. Image reconstruction in higher

dimension: Myocardial perfusion imaging of tracer dynamics with cardiac motion due to deformation and respiration. *Phys Med Biol.* 2015;60(21):8275-8301.

30. Kadrmas DJ, Gullberg GT. 4D maximum a posteriori reconstruction in dynamic SPECT using a compartmental model-based prior. *Phys Med Biol*. 2011;46(5):1553-1574.

31. Abdalah M. 4D Dynamic Image Reconstruction for Cardiac SPECT. *Ph.D. Dissertation, Florida Institute of Technology,* Melbourne, Florida, 2015.

32. Zan Y, Boutchko R, Huang Q, Li B, Chen K, Gullberg GT. Fast direct estimation of the blood input function and myocardial time activity curve from dynamic SPECT projections via reduction in spatial and temporal dimensions. *Med Phys*. 2013;40(9):092503.

33. Gullberg GT, Reutter BW, Sitek A, Maltz JS, and Budinger TF. Dynamic single photon emission computed tomography basic principles and cardiac applications. *Phys Med Biol.* 2010;55(20):111–191.

34. Shrestha U, Scimmarella M, Alhassen A, et al. Measurement of absolute myocardial blood flow in humans using dynamic cardiac SPECT and 99mTc-tetrofosmin: Method and validation. *J Nucl Cardiol.* 2017;24(1):268-277.

35. Kadrmas DJ, DiBella EVR, Huesmanddag RH, and Gullberg GT. Analytical propagation of errors in dynamic SPECT: estimators, degrading factors, bias and noise. *Phys Med Biol.* 1999;44(8):1997-2014

36. Ito K, Jin B, and Takeuchi T. A regularization parameter for nonsmooth tikhonov regularization. SIAM Journal on Scientific Computing, vol. 33, no. 3, pp. 1415{1438, 2011. [Online]. Available: http://epubs.siam.org/doi/abs/10.1137/100790756

37. Eiland D, Mitra D, Abdalah M, Butchko R, and Gullberg GT. SinoCor: Inter-frame and Intra-frame motion correction tool. IEEE Nuclear Science Symposium and Medical Imaging Conference, Anaheim, CA, 2012.

38. Otsu N. A threshold selection method from gray-level histograms. *IEEE Trans Syst, Man, Cybern, Syst.* 1979;9 (1): 62–66.

39. Reutter BW, Gullberg GT, and Huesman RH. Effects of temporal modelling on the statistical uncertainty of spatiotemporal distributions estimated directly from dynamic Cone-beam SPECT projections. *IEEE Trans Med Imag.* 2002;47(15):2673-2683.

40. Reutter BW, Huesman RH, Boutchko R, Brennan KM, Hanrahan SM, and Gullberg GT. Longitudinal evaluation of fatty acid metabolism in normal and spontaneously hypertensive rat hearts with dynamic Micro-SPECT imaging. *Internl Jnl Mol Imag.* 2002;54(11):1938-1945.

740 **41.** Sitek A, Gullberg GT, and Huesman RH. Correction for ambiguous solutions in
741 factor analysis using a penalized least squares objective. *IEEE Trans Med*
742 *Imag.* 2002;21(3):216–225.
743 **42.** Dong W, Li X, Zhang L, and Shi G. 2011 “Sparsity-based image denoising via
744 dictionary learning and structural clustering.” *Proc. IEEE Conf. Computer*
745 *Vision Pattern Recognition*, pp. 457–464.
746 **43.** Aharon M, and Elad M. Sparse and redundant mdeling of image content using
747 an image-Signature-dictionary. *SIAM Jnl Imag. Sciences.* 2008;1(3):228–247.
748 **44.** Levitan E, and Herman GT. A maximum a posteriori probability Expectation
749 Maximization Algorithm for image reconstruction in Emission Tomography.
750 *IEEE Trans Med Imag.* 1989;6(3):185-192.
751 **45.** Choksi R, van Gennip Y, and Oberman A. Anisotropic Total Variation
752 regularized L1-approximation and denoising/deblurring of 2D bar codes.
753 *Inverse Probl Imaging*. 2011;5(3):591-617.
754 **46.** Branham RL, Jr. Alternatives to least squares. *Astron J.* 1982;87(6):928–937.
755 **47.** Segars WP, Sturgeon G, Mendonca S, Grimes J, and Tsui BMW. 4D XCAT
756 phantom for multimodality imaging research. *Med. Phys.* 2010;37(9):4902-
757 4915.
758 **48.** http:/cs.fit.edu/~dmitra/ConvergencePaperSupplement/ -- online repository
759 of 4D reconstruction results for the two algorithms for all examples
760 considered in this paper.
761
762